



# Selective photoredox activity on specific facet-dominated TiO<sub>2</sub> mesocrystal superstructures incubated with directed nanocrystals

Peng Zhang<sup>a</sup>, Takashi Tachikawa<sup>b,c,\*</sup>, Zhenfeng Bian<sup>a,d</sup>, Tetsuro Majima<sup>a,\*\*</sup>

<sup>a</sup> The Institute of Scientific and Industrial Research (SANKEN), Osaka University, Mihogaoka 8-1, Ibaraki, Osaka 567-0047, Japan

<sup>b</sup> Department of Chemistry, Graduate School of Science, Kobe University, 1-1 Rokkodai-cho, Nada-ku, Kobe 657-8501, Japan

<sup>c</sup> PRESTO, Japan Science and Technology Agency (JST), 4-1-8 Honcho Kawaguchi, Saitama 332-0012, Japan

<sup>d</sup> Department of Chemistry, Shanghai Normal University, Shanghai 200234, People's Republic of China

## ARTICLE INFO

### Article history:

Received 6 April 2015

Received in revised form 21 April 2015

Accepted 25 April 2015

Available online 29 April 2015

### Keywords:

TiO<sub>2</sub> mesocrystals

Photoredox activity

Crystal face dependence

## ABSTRACT

The photocatalytic performance of nanocrystalline TiO<sub>2</sub> is crucially influenced by specific facet-induced adsorption and charge separation. Herein, different morphologies of anatase TiO<sub>2</sub> mesocrystal superstructures with directed nanocrystal assembly were controllably synthesized by introducing NH<sub>4</sub>F as an orientation-directing agent. The ratio of the basal and lateral external surfaces of mesocrystals was tuned from 1.1 to 5.8 by increasing the amount of NH<sub>4</sub>F, along with that of {001} and {101} facets of incubated TiO<sub>2</sub> nanocrystals from 0.56 to 0.76. With increasing the ratios, the mesocrystal superstructures exhibited higher photo-oxidation activities in the degradation of 4-chlorophenol (by 1.7 times) and lower activities in Cr<sup>6+</sup> reduction (by 0.47 times) and H<sub>2</sub> generation (by 0.32 times). The H<sub>2</sub> production from dye-sensitized TiO<sub>2</sub> mesocrystal using eosin Y (pH 10) and Ruthenizer 470 (pH 3) are further identify the dominant facets in photocatalysis. It was confirmed that the mesocrystal superstructures with higher ratio of {001}/{101} are more effectively (by 6 times) adsorbed the dye sensitizers under acidic conditions and enhanced charge separation by efficient electron migration through the incubated nanocrystal network and crystal-facet-specific modification of the Pt cocatalyst. The synergetic crystal-facet engineering between mesocrystals and incubated nanocrystals will significantly improve the efficiencies and selectivities of semiconductor photocatalysts.

© 2015 Elsevier B.V. All rights reserved.

## 1. Introduction

Surface science is a critical factor in the equilibrium crystallography and physicochemical performances of semiconductors [1–4]. Thus, anisotropic crystal engineering is becoming an important strategy for tuning and optimizing material reactivities [5–9]. Semiconductor photocatalysts with specific exposed facets exhibit pronounced redox behaviors because of their abundant adsorption sites, efficient separation of photogenerated charges (electrons and holes) and synergism [10–17]. TiO<sub>2</sub> has been widely investigated as an attractive active photocatalyst for environmental and

energy applications [18–22], in which the photocatalytic activity is always dominated by its crystal phase, size, morphology and surface structure [23–26]. Surface-structure control of the atomic configuration can induce anisotropic crystal growth because of the different surface energies. In the case of anatase TiO<sub>2</sub>, the average surface energies of the different facets are 0.90, 0.53 and 0.44 J m<sup>−2</sup> for the (001), (100) and (101) facets, respectively [27]. Based on the Wulff construction, the {001} facet is the most difficult to expose in crystal growth, because its surface energy is higher than that of the thermodynamically stable {101} facet [1]. However, fluorine-ion capping, which is a pioneering development in the synthesis of anisotropic TiO<sub>2</sub> crystals, can reduce the surface energy to 0.51 J m<sup>−2</sup> and largely expose the {001} facets to 47% [17]. As expected, the high-energy {001} facets exhibit higher chemical activities in the degradation of organic pollutants and water splitting compared with {101} facet [28–32]. Meanwhile, some controversial results suggesting that the activity of the {101} facet for specific reactions is superior to that of the exposed {001} facet have been reported [33–36]. Recently, we reported a new strategy for achieving efficient charge separation by site-specific modifica-

\* Corresponding author at: Department of Chemistry, Graduate School of Science, Kobe University, 1-1 Rokkodai-cho, Nada-ku, Kobe 657-8501, Japan. Tel.: +81 78 803 5736; fax: +81 78 803 5736.

\*\* Corresponding author at: The Institute of Scientific and Industrial Research (SANKEN), Osaka University, Mihogaoka 8-1, Ibaraki, Osaka 567-0047, Japan. Tel.: +81 668798495; fax: +81 668798499.

E-mail addresses: [tachikawa@port.kobe-u.ac.jp](mailto:tachikawa@port.kobe-u.ac.jp) (T. Tachikawa), [majima@sanken.osaka-u.ac.jp](mailto:majima@sanken.osaka-u.ac.jp) (T. Majima).

tion of sensitizers and cocatalysts to develop versatile plasmonic photocatalysts, where Au and Pt nanoparticles were loaded on the basal and lateral surfaces of TiO<sub>2</sub> mesocrystals (TMCs) with dominant {001} and {101} facets, respectively [37]. Mesocrystals are assigned to superstructures with a crystallographically ordered alignment of nanoparticles and are useful for many areas of application owing to their unique characteristics, such as high surface area, pore accessibility, electronic conductivity and thermal stability [38–40]. Fundamental mechanistic studies are therefore, needed to gain a proper understanding of the photochemical behavior on TMCs.

Herein, we describe a new approach for the synthesis of a series of TMCs with different morphologies and explore their photocatalytic performance in pollutant degradation and H<sub>2</sub> evolution from water. The ratios of the basal and lateral external surfaces of mesocrystals as well as the shapes of the nanocrystal building blocks were successfully controlled using a crystal growth inhibitor (NH<sub>4</sub>F). It is suggested that the {101} facets prefer reduction, whereas the {001} facets favor oxidation, because of crystal-facet-dependent surface adsorption and charge transfer. This work will help us to gain an in-depth understanding of charge separation within solid catalysts with specific crystal facets and facilitate construction of efficient photocatalysts for environmental and energy conversion applications.

## 2. Experimental

### 2.1. Preparation of TMCs with different morphologies

TMCs with different morphologies were prepared from precursor solutions containing NH<sub>4</sub>F (Wako Pure Chemical Industries), TiF<sub>4</sub> (Sigma–Aldrich), H<sub>2</sub>O, NH<sub>4</sub>NO<sub>3</sub> (Wako Pure Chemical Industries) and P123 [amphiphilic triblock copolymer, namely (EO)<sub>20</sub>(PO)<sub>70</sub>(EO)<sub>20</sub>; Sigma–Aldrich]. The NH<sub>4</sub>F:TiF<sub>4</sub>:H<sub>2</sub>O:NH<sub>4</sub>NO<sub>3</sub>:P123 molar ratios were x:93:32000:453:1. The detailed synthetic procedure and formation mechanism for TMCs have been described elsewhere [37,41]. The obtained samples were denoted by TMC-*n*, where *n* = 1–4, representing the TMCs synthesized with x(NH<sub>4</sub>F) = 0, 46, 116 and 232, respectively. The precursor solutions were placed on a silicon wafer to form a thin layer; the temperature was raised at a rate of 10 °C min<sup>−1</sup> and the solutions were calcined at 500 °C for 2 h. The obtained powders were calcined at 500 °C in an oxygen atmosphere for 8 h to remove surface residues, including fluorine species, completely [42]. The crushed TMCs were prepared by grinding with a mortar before modification.

### 2.2. Preparation of Pt/TMCs

A photochemical deposition method was used to load 1 wt% Pt nanoparticles on TMCs with different morphologies [43]. In a typical procedure, TMCs (30 mg), Milli-Q ultrapure water (27 mL; Millipore), methanol (3 mL) and a certain amount of H<sub>2</sub>PtCl<sub>6</sub> (Aldrich) were mixed to form a homogeneous suspension. The solution was then exposed to ultraviolet (UV) light from a mercury light source (Asahi Spectra, REX-250) for 30 min at room temperature. Finally, the product was collected after centrifugation and dried. The amount of loaded Pt was determined using inductively coupled plasma atomic emission spectroscopy (Shimadzu, ICPS-8100).

### 2.3. Characterization

The crystal structures of the samples were examined using X-ray diffraction (XRD; Rigaku, Smartlab; operated at 40 kV and 200 mA, Cu Kα source). The morphologies were investigated using

field-emission scanning electron microscopy (FESEM; JEOL, JSM-6330FT) and transmission electron microscopy (TEM; JEOL, JEM 3000F operated at 300 kV or Hitachi, H-800 operated at 200 kV). The Brunauer–Emmett–Teller (BET) surface areas were measured using nitrogen sorption (BEL Japan, BEL-SORP max). The pore volumes and pore diameter distributions were derived from the adsorption isotherms, using the Barrett–Joyner–Halenda (BJH) model. The UV–vis diffuse reflectance spectra were measured using UV–vis–NIR spectrophotometers (Jasco, V-570) at room temperature.

### 2.4. Photocatalytic degradation test

For a typical photocatalytic process, TMC dispersions (2 mL) containing 4-chlorophenol (Wako Pure Chemical Industries) (0.1 mM) or K<sub>2</sub>Cr<sub>2</sub>O<sub>7</sub> (Wako Pure Chemical Industries) (0.4 mM) were sonicated for 20 min and then transferred to a quartz cuvette. The photocatalytic reaction was initiated by irradiation with a mercury light source (Asahi Spectra, REX-250) through a filter (centered at 365 nm) at room temperature. After stopping the UV illumination, the sample was centrifuged at 10,000 rpm (Hitachi, Himac CF16RX) to separate the solid particles. The concentration of unreacted molecules, from which the degradation yield was calculated, was analyzed using a UV–vis–NIR spectrophotometer (Shimadzu, UV-3100 or UV-3600) at the characteristic wavelength.

### 2.5. Photocatalytic H<sub>2</sub> generation test

For UV-induced H<sub>2</sub> production, Pt/TMC (2.5 mg) was suspended in 5 vol% methanol–water (5 mL). Ar was bubbled through the suspension for 20 min, and then the test tube was sealed with a rubber septum. The test tube was irradiated with a mercury light source (Asahi Spectra, REX-250) through a filter (centered at 365 nm), with magnetic stirring, at room temperature. The intensity of the UV light was approximately 100 mW cm<sup>−2</sup>. For visible-light H<sub>2</sub> production, Pt/TMC (2.5 mg) was dispersed in 5 mL of an aqueous solution (pH 10, adjusted with NaOH and HCl) of 1 mM eosin Y (EY<sup>2−</sup>; Nacalai Tesque) and 0.7 M triethanolamine (TEOA; Sigma–Aldrich), or in 5 mL of an aqueous solution (pH 3, adjusted with HClO<sub>4</sub>) of 10 μM Ruthenizer 470 (Solaronix) and 10 mM ethylene-diaminetetraacetic acid (EDTA; Nacalai Tesque). The suspensions were irradiated with visible light (Asahi Spectra, HAL-C100; 400–700 nm, 100 mW cm<sup>−2</sup>), with magnetic stirring, at room temperature. A 430 nm cutoff filter was used to remove UV light. After the reaction, the gas (0.1 mL) was collected from the top of the reactor and analyzed using a Shimadzu GC-8A gas chromatograph equipped with an MS-5A column and a thermal conductivity detector. The surface concentrations of the dye sensitizers were determined from the UV–vis absorption spectra of supernatant solutions separated by centrifugation.

### 2.6. Time-resolved diffuse reflectance measurements

Ar-saturated acetonitrile slurries containing the catalyst powders (20 g L<sup>−1</sup>) and N719 ruthenium dye [*cis*-diisothiocyanato-bis(2,2′-bipyridyl)-4,4′-dicarboxylato] ruthenium(II) bis(tetrabutylammonium), 1 mM; Solaronix] were prepared. Time-resolved diffuse reflectance measurements were performed using the second harmonic generation (532 nm, 0.2 mJ pulse<sup>−1</sup>, 5 ns full-width at half-maximum) from a Q-switched Nd<sup>3+</sup>: YAG laser (Continuum, Surelite II-10) for excitation, operated with temporal control by a delay generator (Stanford Research Systems, DG535). The reflected analyzing light from a continuous-wave 450 W Xe-arc lamp (Ushio, UXL-451-0) was collected using a focusing lens and directed through a grating monochromator (Nikon, G250) to a silicon avalanche photodiode

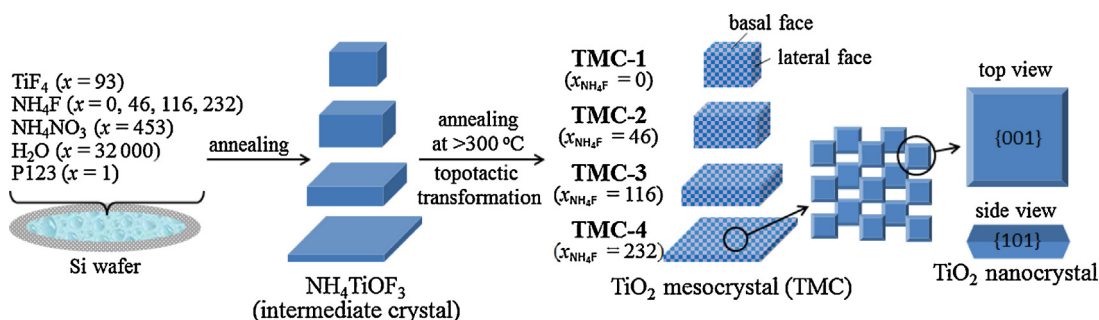


Fig. 1. Synthesis of different-shaped  $\text{TiO}_2$  mesocrystals (TMCs) with various ratios of  $\{001\}/\{101\}$ .

detector (Hamamatsu Photonics, S5343). The transient signals were amplified with a voltage amplifier (Femto, DHPVA-100) and recorded using a digitizer (Tektronix, DPO3054). All experiments were carried out at room temperature. The percentage absorption (%abs) is given by the equation:  $\%abs = [(R_0 - R)/R_0] \times 100$ , where  $R$  and  $R_0$  represent the intensities of the diffuse reflected monitor light with and without excitation, respectively.

### 3. Results and discussion

#### 3.1. Synthesis and structure of different-shaped TMCs

The synthesis and structures of different-shaped TMCs are shown in Fig. 1. A thin layer of an aqueous solution containing  $\text{TiF}_4$ ,  $\text{NH}_4\text{NO}_3$ , P123 and  $\text{NH}_4\text{F}$  was dropped on a silicon wafer and calcined at  $500^\circ\text{C}$ . Intermediate  $\text{NH}_4\text{TiO}_3$  crystals were formed during the initial annealing process ( $<200^\circ\text{C}$ ), as indicated by powder XRD patterns (Fig. S1) [42,44]. During the self-assembly process, the amount of  $\text{NH}_4\text{F}$  added was critical in controlling the size and thickness of the crystal (FESEM images of intermediate  $\text{NH}_4\text{TiO}_3$  crystals in Fig. S2) [41]. With increasing annealing temperatures, topotactic transformation occurred from  $\text{NH}_4\text{TiO}_3$  to anatase  $\text{TiO}_2$ . It has been reported that the plate-like mesocrystal superstructures are composed of aligned anatase  $\text{TiO}_2$  nanocrystals with dominant  $\{001\}$  facets which lead to efficient charge separation over

4 times than nanocrystals system [42,45]. When the molar ratio  $x$  of  $\text{NH}_4\text{F}$  relative to that of P123 was in the range 0–232, the growth geometry was well ordered along the  $[101]$  zone axis. Under variable conditions, the TMC morphology gradually became thinner and longer, i.e., the proportion of basal surfaces with dominant  $\{001\}$  facets increased and that lateral surfaces with dominant  $\{101\}$  facets decreased. The low-magnification FESEM images in Fig. 2 show the general morphologies of the as-synthesized TMCs. The TMC shape was changed from cubic to plate-like by varying the molar ratio of  $\text{NH}_4\text{F}$ , although some agglomerates were occasionally observed. As can be seen in Fig. 2a, cubic structures of average thickness  $\sim 290$  nm and average size  $\sim 650$  nm were formed in the absence of  $\text{NH}_4\text{F}$ . With increasing the amount of  $\text{NH}_4\text{F}$ , the average TMC thickness decreased and the average length increased (Fig. 2b–d). Eventually, increasing the concentration of  $\text{NH}_4\text{F}$  produced a sheet-like structure with a thickness of  $\sim 120$  nm. When we further increased the  $\text{NH}_4\text{F}$  concentration, the TMC sheets merged to form irregular structures, because of the excess area of the  $\{001\}$  surfaces. Based on the gradual changes in the morphology from cubic to plate-like structures, the area ratios of the basal surfaces to the lateral surfaces ( $S_{\text{basal}}^M/S_{\text{lateral}}^M$ ) vary from 1.1 to 5.8 (Table 1), where  $M$  indicates the external surface of a mesocrystal to distinguish it from nanocrystal facets. Likewise, the area ratios of the  $\{001\}$  and  $\{101\}$  facets of  $\text{TiO}_2$  nanocrystals in TMCs ( $S_{\{001\}}^N/S_{\{101\}}^N$ ) clearly increased from 0.56 to

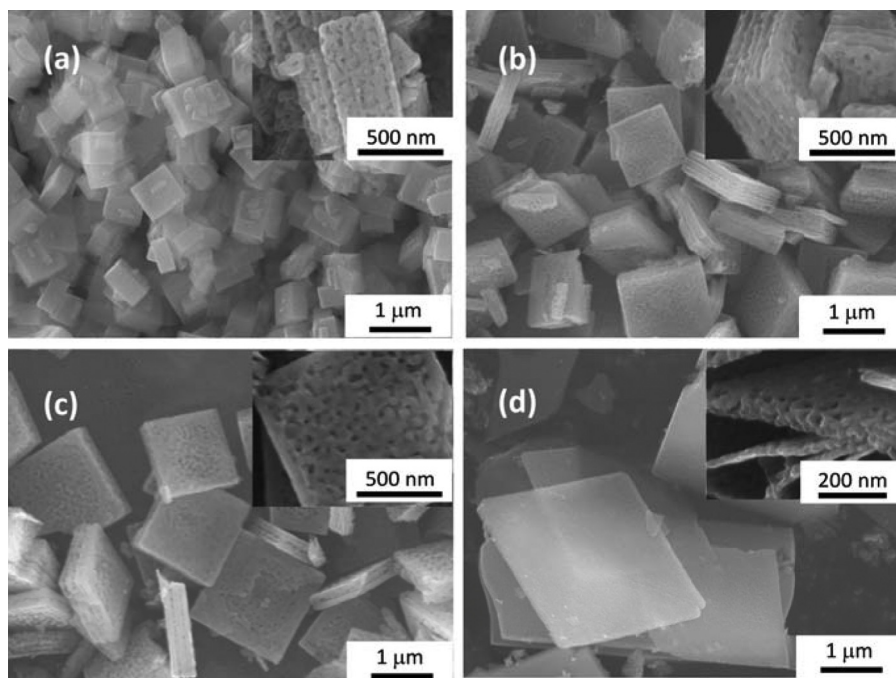
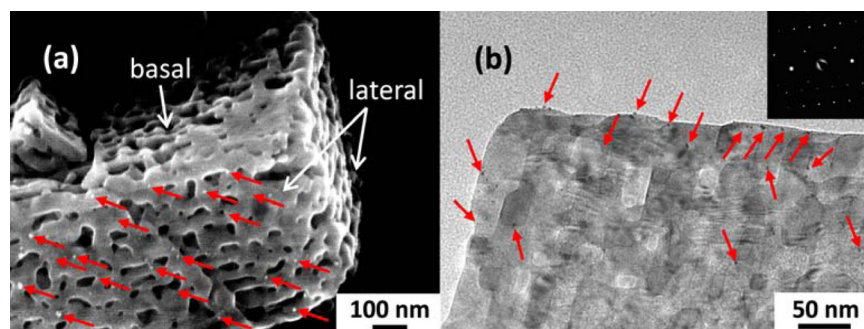


Fig. 2. FESEM images of different-shaped TMCs synthesized with  $x$  (molar ratio of  $\text{NH}_4\text{F}$ ) = 0 (a), 46 (b), 116 (c) and 232 (d). Insets show the high-magnification FESEM images.





**Fig. 3.** (a) High-magnification FESEM image of Pt/TMC-1. (b) TEM image of Pt/TMC-4. The red arrows indicate the Pt nanoparticles. Inset in panel (b) indicates the electron diffraction pattern of the selected area. (For interpretation of the references to color in this figure legend, the reader is referred to the web version of this article.)

0.76 by increasing the amount of  $\text{NH}_4\text{F}$  (Table 1), supporting our explanation that  $\text{NH}_4\text{F}$  mainly controls the shapes of the  $\text{NH}_4\text{TiOF}_3$  intermediate crystals and resultant TMCs and even the alignment nanocrystals.

Electron microscope analyzes further confirmed the superstructures of the TMC samples. The high-magnification FESEM and TEM images clearly show that the TMCs have a typical porous structure with a pore size of several tens of nanometers (Fig. 3). A selected-area electron diffraction pattern recorded on the TMC shows a diffraction pattern corresponding to single-crystal anatase along the  $[001]$  zone axis; this indicates ordered alignment of nanocrystals (inset in Fig. 3b). A photochemical deposition technique was used to prepare Pt-nanoparticle-loaded TMCs [43]. In Fig. 3a and b, a number of Pt nanoparticles (red arrows) are clearly seen on the TMC surfaces. It is worth noting that the Pt nanoparticles are mostly deposited on the lateral faces of the TMCs and the pore wall surfaces; these exposed  $\{101\}$  facets as reductive sites [45]. The preferential deposition of Pt nanoparticles on the  $\{101\}$  facets has previously been observed for anatase  $\text{TiO}_2$  nanocrystals [15,16,43]. The size distributions of the Pt nanoparticles deposited on the TMCs are between 1.5 and 3.5 nm, with average diameters of  $\sim 2.5$  nm (Fig. S4).

The powder XRD patterns of as-synthesized TMCs are shown in Fig. 4a. All the diffraction peaks are attributable to the anatase phase of  $\text{TiO}_2$  with good crystallinity. There are no obvious differences between the peak positions and peak widths with and without  $\text{NH}_4\text{F}$ . For anatase  $\text{TiO}_2$ , the detected main peaks at  $2\theta$  values of  $25.8^\circ$ ,  $37.7^\circ$  and  $47.8^\circ$  can be assigned to the (101), (004) and (200) planes, respectively, in the tetragonal anatase phase. The crystallinity of the samples is not significantly different. Meanwhile, the relative ratio of the (004) diffraction peak intensity to that of the (101) peak increased with increasing the  $\text{NH}_4\text{F}$  concentration, implying oriented crystal growth along the  $[101]$  zone axis (Table 1). This tendency is in good agreement with the FESEM results. In addition, the crystallite sizes of  $\text{TiO}_2$  estimated from the Scherrer equation are consistent with the TEM observations (Table 1).

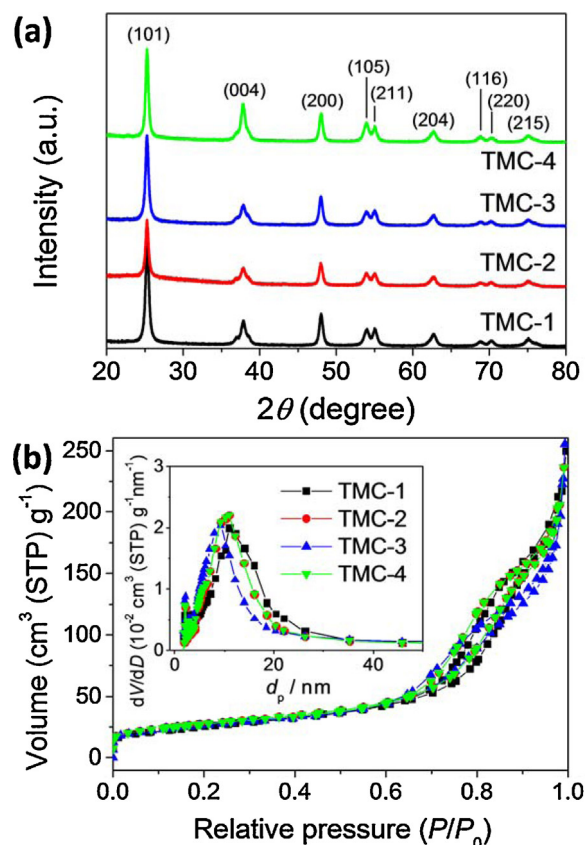


**Fig. 4.** (a) Powder XRD patterns and (b) nitrogen adsorption-desorption isotherms and pore size distributions (inset) of TMCs.

Fig. 4b shows the nitrogen adsorption-desorption isotherms and the corresponding pore-size distribution curves (inset) for the TMC samples. All the curves show type IV isotherms and hysteresis loops at high relative pressures, supporting the presence of meso-

**Table 1**  
Structural characteristics of  $\text{TiO}_2$  mesocrystals (TMCs).

Sample	Thickness [nm] <sup>a</sup>	Length [nm] <sup>b</sup>	$S_{\text{basal}}^M/S_{\text{lateral}}^M$	$I_{(001)}/I_{(004)}^c$	Surface area [ $\text{m}^2 \text{g}^{-1}$ ]	Pore volume [ $\text{cm}^3 \text{g}^{-1}$ ]	Pore size [nm]	Nanocrystal size [nm] <sup>d</sup>	$S_{(001)}^N/S_{(101)}^N$ <sup>e</sup>
TMC-1	290	650	1.1	0.22	92	0.29	11	19 (21)	0.56
TMC-2	210	880	2.1	0.24	96	0.36	11	21 (22)	0.59
TMC-3	140	1000	3.6	0.25	93	0.36	9	24 (21)	0.67
TMC-4	120	1400	5.8	0.44	96	0.36	11	23 (22)	0.76

<sup>a</sup> Face-to-face distance between basal facets of TMC.

<sup>b</sup> Face-to-face distance between lateral facets of TMC.

<sup>c</sup> Obtained from powder XRD data; see the text for details.

<sup>d</sup> Obtained from TEM analysis; see the ESI for the calculation (Fig. S3 and Table S1). The numbers in parentheses are the nanocrystal size calculated from powder XRD data using the Scherrer equation.

<sup>e</sup> Ratio of surface areas of nanocrystals in TMCs, determined from TEM analysis; see the Supporting information for the calculation (Fig. S3 and Table S1).

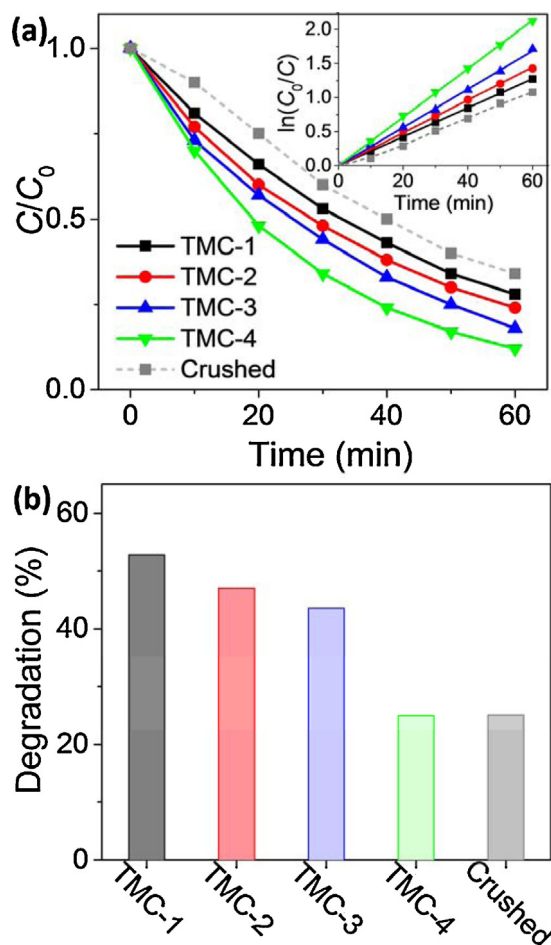


**Fig. 5.** Photocatalytic degradation of (a) 4-chlorophenol ( $[TMC] = 0.5 \text{ g L}^{-1}$ ,  $[4\text{-chlorophenol}] = 0.1 \text{ mM}$ , pH 7,  $\lambda = 365 \text{ nm}$ ,  $I_{UV} = 140 \text{ mW cm}^{-2}$  and air saturation,) and (b)  $Cr^{6+}$  in aqueous phase ( $[TMC] = 0.4 \text{ g L}^{-1}$ ,  $[Cr^{6+}] = 0.4 \text{ mM}$ , pH 3,  $\lambda = 365 \text{ nm}$ ,  $I_{UV} = 100 \text{ mW cm}^{-2}$ ,  $t_{UV} = 2 \text{ h}$  and air saturation,) over different TMC samples under UV-light irradiation.

porous structures. The pore-size distributions in the Fig. 4b inset indicate that all the samples have mesopores with mean sizes of around 10 nm. Furthermore, the BET specific surface areas of the samples are very similar ( $\sim 90 \text{ m}^2 \text{ g}^{-1}$ ) (Table 1), although the sample morphologies are quite different.

### 3.2. Photocatalytic degradation under UV-light irradiation

All samples of TMCs are responded to UV light absorption due to their intrinsic band gap (Fig. S5). The photocatalytic performances of TMCs with different morphologies in the oxidative degradation of 4-chlorophenol, which is a commonly used test compound for photocatalysis [42], were evaluated. Fig. 5a shows the degradation of 4-chlorophenol under UV-light irradiation, where  $C_0$  and  $C$  are the concentrations of 4-chlorophenol before and after UV-light irradiation, respectively. Negligible degradation was observed in the absence of TMCs or UV light. The rate constants for 4-chlorophenol degradation were estimated from the slopes of  $\ln(C_0/C)$  vs. irradiation time (inset in Fig. 5a) to be 0.021, 0.024, 0.028 and  $0.036 \text{ min}^{-1}$  for TMC-1–4, respectively. The degradation efficiency clearly increased from 72% to 88% in proportion to the amount of  $\{001\}$  surfaces. Eventually, the TMC-4 exhibited the highest activity among the samples tested. This result indicates that the reactive  $\{001\}$  facets play a crucial role in the photodegradation of 4-chlorophenol, possibly because of their strong ability to form hydroxyl radicals [28].

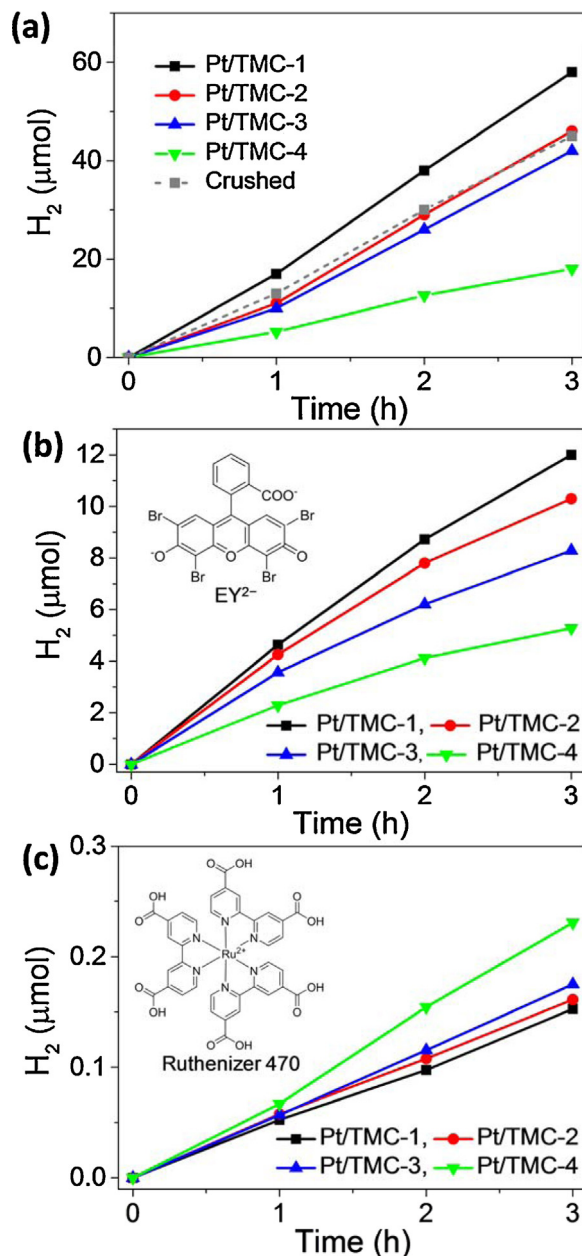


**Fig. 6.**  $H_2$  evolution during (a) UV-light ( $\lambda = 365 \text{ nm}$ ,  $I_{UV} = 100 \text{ mW cm}^{-2}$ ) and (b and c) visible-light ( $\lambda = 430 \sim 700 \text{ nm}$ ,  $I_{vis} = 100 \text{ mW cm}^{-2}$ ) irradiation of Pt/TMC samples ( $0.5 \text{ g L}^{-1}$ ) in Ar saturated solution containing (a) 5% methanol, (b) 1 mM eosin Y (EY) ( $0.7 \text{ M TEOA}$ ; pH 10) (c) 10  $\mu\text{M}$  Ruthenizer 470 (10 mM; EDTA pH 3).

To further evaluate the TMC performances, we examined the photocatalytic reduction of  $Cr^{6+}$  in the aqueous phase as a probe reaction. The changes in the characteristic absorption bands were monitored to estimate the degradation efficiency. In contrast to oxidative degradation, the activity increased from 25% to 53% in the order  $TMC-4 < TMC-3 < TMC-2 < TMC-1$ , as shown in Fig. 5b.

### 3.3. Photocatalytic $H_2$ evolution under UV-light irradiation

As is well known, pure  $TiO_2$  cannot split water effectively to produce  $H_2$  under UV-light irradiation. The reaction efficiency of this process is improved when a Pt cocatalyst and sacrificial electron donor are added to the system [46,47]. We measured the amounts of  $H_2$  evolved during UV-light irradiation of the Pt/TMC powders in aqueous solutions containing methanol as a sacrificial

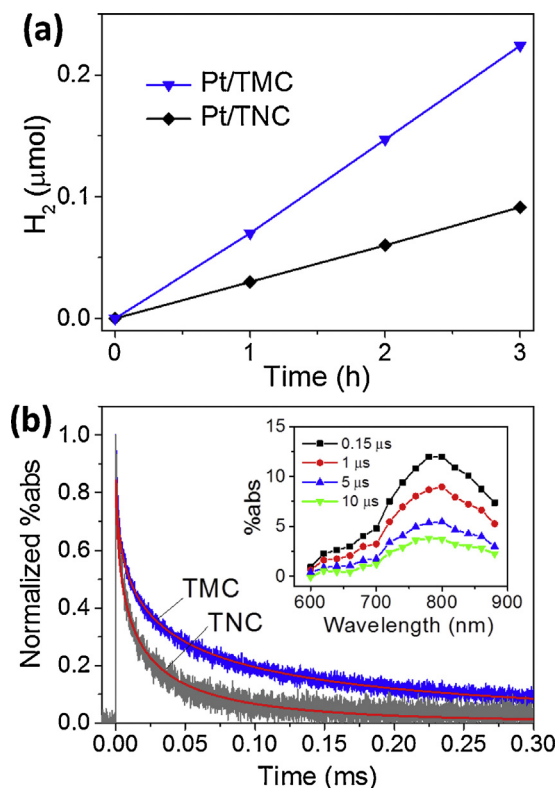


**Fig. 7.** (a) H<sub>2</sub> evolution during visible-light irradiation of Pt/TMC and Pt/TNC powders suspended in aqueous solutions containing Ruthenizer 470 and EDTA. The experimental conditions were [catalyst] = 0.5 g L<sup>-1</sup>, [Ruthenizer 470] = 10 μM, [EDTA] = 10 mM, pH 3, λ = 430–700 nm, I<sub>vis</sub> = 100 mW cm<sup>-2</sup>, and initial Ar saturation. (b) Time traces of transient absorption observed at 827 nm during the 532-nm laser flash photolysis of acetonitrile suspensions of TMCs and TNCs in the presence of N719 dye. The red lines were obtained using Eq. (4). Inset shows the time-resolved diffuse reflectance spectra obtained for acetonitrile suspensions containing TMCs and N719 dye. (For interpretation of the references to color in this figure legend, the reader is referred to the web version of this article.)

electron donor. Fig. 6a shows the time profiles of H<sub>2</sub> evolution over Pt/TMC samples with different morphologies. Interestingly, the photocatalytic activity increased with decreasing  $S_{\text{basal}}^{\text{M}}/S_{\text{lateral}}^{\text{M}}$  and  $S_{\{001\}}^{\text{N}}/S_{\{101\}}^{\text{N}}$ ; for example, the activity of Pt/TMC-1 was 2.5 times than that of Pt/TMC-4. Pan et al. [33] and Gordon et al. [34] reported that TiO<sub>2</sub> nanocrystals with dominant {101} facets produce more H<sub>2</sub> than {001} faceted crystals do; this is in agreement with our results. It is therefore, proposed that following UV-light irradiation, the photogenerated electrons in the conduction band (CB) of TiO<sub>2</sub> migrate from the {001} facet to the {101} facet and are stored in Pt, where they reduce H<sup>+</sup> to generate H<sub>2</sub> [35]. Concurrently, the photogenerated holes, which could be preferentially trapped on the {001} facet, oxidize the methanol.

To verify the superior properties of superstructures, we compared the photocatalytic activities of TMC-1 with their crushed structures (TEM image in Fig. S6). As comparison between the ordered and crushed case, these latter samples exhibited more than 20% lower activity than their intact ones in aforementioned series of reactions (Figs. 5 and 6a). Therefore, the TMCs with well-aligned nanocrystals can efficiently promote the photoactive efficiency due to the facilitative of charge separation, which is consistent with reported results [42].

#### 3.4. Dye-sensitized H<sub>2</sub> evolution under visible-light irradiation

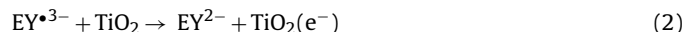
Efficient sunlight harvesting from UV to visible regions is one of the key challenges for practical applications. We thus, examine

the differences among facet-dominated reactions in dye-sensitized water-splitting systems [48–52]. The efficiency of H<sub>2</sub> evolution in the presence of visible-light-active dye sensitizers is determined by the following factors: (i) surface adsorption of dyes, (ii) interfacial electron transfer from the excited dyes (or reducing dye radical anions) to the CB of TiO<sub>2</sub>, and (iii) charge recombination between the oxidized dyes and injected electrons. Using dye sensitizers of EY [49] and Ruthenizer 470 [48] to investigate the factor (i), the efficiencies of visible-light-active H<sub>2</sub> evolution were tested on series of TMCs with specific dominant-facets.

Fig. 6b shows the time dependence of H<sub>2</sub> production during visible-light irradiation of aqueous suspensions of Pt/TMC powders in the presence of EY (its molecular structure is shown in the inset Fig. 6b) and TEOA, which was used as a sacrificial electron donor. It is obvious that all the Pt/TMC samples evolved H<sub>2</sub> at the same level as the previously reported one [49] and their activities increased as  $S_{\text{basal}}^{\text{M}}/S_{\text{lateral}}^{\text{M}}$  and  $S_{\{001\}}^{\text{N}}/S_{\{101\}}^{\text{N}}$  decreased.

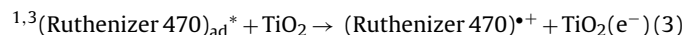
The pK<sub>a</sub> values for proton dissociation of the hydroxyl and carboxylic groups of EY in water are 2.81 and 3.75, respectively [53], therefore EY forms a dianion (EY<sup>2-</sup>) in alkaline solution at pH 10. Anatase TiO<sub>2</sub> nanoparticles have an isoelectric point in the vicinity of pH 6–7 [54], implying that molecular adsorption is strongly inhibited by repulsion between negatively charged TiO<sub>2</sub> and EY<sup>2-</sup> [49]. In fact, the concentrations of adsorbed EY molecules on the Pt/TMC samples were estimated to be below 1% of the total EY.

The reaction process after photoexcitation of free EY<sup>2-</sup> in solution is summarized as follows:



where  ${}^1,3(\text{EY}^{2-})^*$  are EY<sup>2-</sup> in the singlet and triplet excited states and TEOA<sup>•+</sup> is TEOA radical cation [55]. Back electron transfer from EY<sup>•3-</sup> to TEOA<sup>•+</sup> would be inhibited because of the rapid degradation of TEOA<sup>•+</sup>. EY<sup>•3-</sup>, which is generated from reductive quenching of  ${}^1,3(\text{EY}^{2-})^*$  by TEOA, ejects an electron to TiO<sub>2</sub> via a collision process. The one-electron reduction potential of EY<sup>2-</sup> was reported to be −0.80 vs. normal hydrogen electrode (NHE) [56], which is higher than the CB level (−0.71 V vs. NHE at pH 10) of TiO<sub>2</sub> [57]. Reaction (2) is therefore, thermodynamically preferable. During this key step, electrons are preferentially injected into the {101} facet, which has a CB level lower by ca. 0.05–0.1 V than that of the {001} facet [58,59]. Finally, electrons are trapped by Pt and consumed in H<sup>+</sup> reduction. This confirms the key role of the {101} facets in determining the reaction efficiency and enables understanding of the activity trend.

Ruthenizer 470 (its molecular structure is shown in the inset in Fig. 6c) has six carboxylic groups, which act as efficient anchors on the TiO<sub>2</sub> surface. In the Ruthenizer-470-sensitized Pt/TMC system (pH 3), the excited dye molecules adsorbed on the TMC surface inject electrons into the CB of the TMC as follows:



where  ${}^1,3(\text{Ruthenizer 470})_{\text{ad}}^*$  is Ruthenizer 470 in the singlet and triplet excited states adsorbed on the TiO<sub>2</sub> surface [48]. The sensitizer is regenerated by an electron donor, i.e., EDTA.

As shown in Fig. 6c, the visible-light H<sub>2</sub> evolution activity of the Pt/TMC samples increased as  $S_{\text{basal}}^{\text{M}}/S_{\text{lateral}}^{\text{M}}$  and  $S_{\{001\}}^{\text{N}}/S_{\{101\}}^{\text{N}}$  increased, in contrast to the EY-sensitized system. The amounts of adsorbed Ruthenizer 470 on the TMC surfaces were estimated to compare the adsorption abilities of the catalysts. It is clearly seen from Fig. S7 that the TMC samples with dominant {001} facets adsorb more dye molecules on their surfaces.

Yu et al. found that the surface concentration ( $1.43 \times 10^{-7}$  mol cm<sup>-2</sup>) of N719 dye [cis-bis(isothiocyanato) bis(2,2'-bipyridyl-4,4'-dicarboxylato) ruthenium(II)]



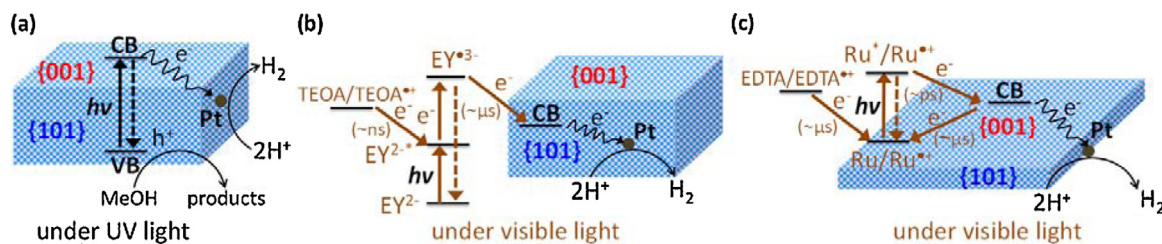


**Fig. 8.** H<sub>2</sub> evolution during (a) UV-light irradiation of Pt/TMC in methanol-water solution, (b) visible-light irradiation of Pt/TMC in aqueous solution (pH 10) containing EY and TEOA and (c) visible light irradiation of Pt/TMC in aqueous solution (pH 3) containing Ruthenizer 470 and EDTA. VB is valence band of TiO<sub>2</sub>. Ru is adsorbed Ruthenizer 470. Typical time scales for electron transfer [55,69–72] are shown below the arrows.

bis(tetrabutylammonium)] adsorbed on TiO<sub>2</sub> nanosheets with dominant {001} facets was slightly lower than that ( $2.14 \times 10^{-7} \text{ mol cm}^{-2}$ ) on typical anatase nanoparticles in acetonitrile electrolyte solution [60]. Laskova et al. also reported that the surface concentration ( $0.4\text{--}0.5 \text{ molecules nm}^{-2}$ ) of C101 dye [cis-bis(isothiocyanate)(4,4'-bis(5-hexylthiophene-2-yl)-2,2'-bipyridyl)-ne](4-carboxylic acid-4'-carboxylate-2,2'-bipyridine) ruthenium-(II) sodium] was lower on TiO<sub>2</sub> (001) nanosheets than that on TiO<sub>2</sub> (101) nanoparticles ( $0.7\text{--}0.8 \text{ molecules nm}^{-2}$ ) [61]. Recent first-principle theoretical calculations suggested that the observed smaller dye coverage on the {001} facets than that on the {101} facets is a consequence of a partial contact of the thiophene and alkyl bipyridine substituents of C101 with the TiO<sub>2</sub> surface [59]. Compared with those systems, Ruthenizer 470 does not have bulky substituents and its surface concentrations on the TMC samples are quite low (e.g.,  $0.023 \text{ molecules nm}^{-2}$  for TMC-4). The effect of steric hindrance by TiO<sub>2</sub> and adsorbed molecules is therefore, explicitly ruled out. According to the literature [62–64], the anatase {001} surface has a strong ability to adsorb hydroxyl and carboxylic groups (as well as water molecules) dissociatively onto the undercoordinated Ti cations. It can therefore, be reasonably concluded that  $S_{\text{basal}}^{\text{M}}/S_{\text{lateral}}^{\text{M}}$  with synergetic nanocrystal engineering plays an essential role in determining the dye adsorption capability, because the surface areas of the TMC samples are very similar.

### 3.5. Charge transfer dynamics on TMCs

To verify the superior properties of TMCs with directed nanocrystal assembly, we compared the photocatalytic activities of TMCs synthesized without P123, which have a similar morphology to TMC-4, and anatase TiO<sub>2</sub> nanocrystals (TNCs) with similar surface areas [42]. The TNCs have a truncated bipyramidal morphology and the percentage of exposed TNC {001} facets is similar to that for TMC [42]. As demonstrated in Fig. 7a, Ruthenizer-470-sensitized TMCs could efficiently produce H<sub>2</sub> under visible-light irradiation than Ruthenizer-470-sensitized TNCs did.

Factors (ii) and (iii), mentioned above, were examined. In general, the metal-to-ligand charge transfer excited states of the adsorbed ruthenium dyes have higher energies than the CB of TiO<sub>2</sub>, suggesting that this interfacial electron transfer is highly exergonic. Our group recently observed, using time-resolved confocal fluorescence spectroscopy, that the average emission lifetimes of an adsorbed ruthenium dye [cis-bis(2,2'-bipyridyl)-(2,2'-bipyridyl-4,4'-dicarboxylic acid) ruthenium(II) hexafluorophosphate] were very similar ( $\sim 25 \text{ ns}$ ) for the {001} and {101} facets of anatase TiO<sub>2</sub> crystals in acetonitrile [65]. Based on this result, it can be assumed that the electron injection efficiencies of the {001} and {101} facets are similar.

The injected electrons in TiO<sub>2</sub> either migrate to Pt or recombine with the oxidized dye. The interparticle charge transfer is an important factor that affects the photocatalytic activity in

**Table 2**

Fitting parameters for decay kinetics.

Sample	$\tau$ [ $\mu\text{s}$ ]	$\alpha$
TMC	27	0.37
TNC	10	0.44

dye-sensitized water-splitting processes [66–68], because the spatial charge separation at the dye–semiconductor interface greatly retards charge recombination between electrons and oxidized dyes. Time-resolved diffuse reflectance spectroscopy [69–70] was used to explore the dynamics of recombination of the injected electrons in the TMCs and the dye cations. As shown in Fig. 7b, the time trace of the transient absorption signal was monitored at 827 nm during the 532-nm laser flash photolysis of TiO<sub>2</sub> powders sensitized with N719 ruthenium dye in Ar-saturated acetonitrile. Electron injection was completed within the laser pulse scattering time (ca. 100 ns) and the accompanying dye cations and injected electrons appeared in the wavelength region above 600 nm (inset in Fig. 7b) [71]. The TNC system showed similar spectral features and electron injection efficiency (Fig. S8). The observed time traces were well reproduced using a stretched exponential function:

$$\% \text{abs}(t) = (\% \text{abs})_0 \exp[-(t/\tau)\alpha] \quad (4)$$

where  $(\% \text{abs})_0$  is the initial absorbance of the dye cations that were generated within the laser pulse (at  $t=0$ ),  $\tau$  is the average lifetime, and  $\alpha$  is a heterogeneous parameter [71]. The fitting parameters are summarized in Table 2. The  $\tau$  of the TMC system was about three times longer than that of the TNC system, supporting the idea that efficient electron transport in the mesocrystal superstructure slows down recombination. This result may explain the higher activity observed for Ruthenizer-470-sensitized TMCs. Moreover, the higher  $\alpha$  value for the TMC system is possibly attributed to more dispersive recombination dynamics through multiple electron trapping/detrapping processes.

### 3.6. Reaction mechanisms

The proposed reaction mechanisms of charge transfer on TMCs are illustrated in Fig. 8. In the case of UV excitation (Fig. 8a), the photogenerated electrons are preferentially trapped on the {101} surface through the nanocrystal network in the TMCs and reduce substances such as Pt precursor and H<sup>+</sup>. Because of high surface energy ( $0.90 \text{ J m}^{-2}$ ), the {001} surfaces effectively adsorb water and alcoholic compounds in a dissociative manner, facilitating their oxidation by photogenerated holes and/or hydroxyl radicals (Fig. 5a). Reduction seems to occur preferentially on the {101} facets rather than on the {001} facets (Figs. 5b and 6a).

Both the dye-sensitized TMC samples tested here act as visible-light-responsive photocatalysts for H<sub>2</sub> evolution, but the reaction processes are quite different. In the EY-sensitized system (Fig. 8b), the electrons are delivered by freely diffusing EY<sup>•3-</sup>, which is generated by electron-transfer reactions between <sup>1,3</sup>(EY<sup>2-</sup>)<sup>\*</sup> and

TEOA. The injected electrons are then transferred to Pt nanoparticles deposited on the TMC {101} facets to produce H<sub>2</sub> (Fig. 6b). In contrast, Ruthenizer 470 is more efficiently adsorbed on the {001} facets up to 3.2  $\mu\text{mol g}^{-1}$  (Fig. S7), therefore, the TMC samples with higher  $S_{\text{basal}}^{\text{M}}/S_{\text{lateral}}^{\text{M}}$  and  $S_{\{001\}}^{\text{N}}/S_{\{101\}}^{\text{N}}$  values exhibit higher activities for H<sub>2</sub> production (Fig. 6c). The electrons directly injected from the excited dyes can avoid charge recombination with the dye cations remaining on the {001} surface because of efficient migration across the assembled nanocrystals interface and reach the Pt cocatalyst on the {101} surface (Fig. 8c).

#### 4. Conclusions

In summary, we developed a new strategy for synthesizing a series of desired TiO<sub>2</sub> mesocrystals superstructures with controlled crystal facets. It was found that mesocrystals with different facet ratios showed different reactivity orders in photo-oxidation, i.e., {001} > {101} (by 1.7 times), and photoreduction, i.e., {101} > {001} (by 2–3 times), under UV-light irradiation, similar to those observed in conventional nanocrystal systems. Furthermore, we examined the visible-light photocatalytic activities of mesocrystals with different morphologies, using EY and ruthenium dyes as sensitizers. It was confirmed that the {001} facets are preferred for molecular adsorption and electron injection from the photoexcited dye sensitizers to the CB of TiO<sub>2</sub>, whereas the {101} facets are favor for the collection of photogenerated electrons, owing to directional electron flow. Our findings highlight that the concept of crystal-facet-dependent photocatalytic reactions can be extended to superstructure systems with well-regulated morphologies. These findings are important in semiconductor physics and chemistry with respect of the construction of versatile solar energy conversion systems.

#### Acknowledgements

A part of TEM measurements was carried out in a facility at Research Center for Ultrahigh Voltage Electron Microscopy, Osaka University. This work has been partly supported by Innovative Project for Advanced Instruments, Renovation Center of Instruments for Science Education and Technology, Osaka University and a Grant-in-Aid for Scientific Research (Project 25220806, 25810114 and others) from the Ministry of Education, Culture, Sports, Science and Technology (MEXT) of the Japanese Government.

#### Appendix A. Supplementary data

Supplementary data associated with this article can be found, in the online version, at <http://dx.doi.org/10.1016/j.apcatb.2015.04.053>.

#### References

- [1] U. Diebold, *Surf. Sci. Rep.* 48 (2003) 53–229.
- [2] T.L. Thompson, J.T. Yates Jr., *Chem. Rev.* 106 (2006) 4428–4453.
- [3] G.A. Somorjai, H. Frei, J.Y. Park, *J. Am. Chem. Soc.* 131 (2009) 16589–16605.
- [4] M.A. Henderson, *Surf. Sci. Rep.* 66 (2011) 185–297.
- [5] Y. Yin, A.P. Alivisatos, *Nature* 437 (2005) 664–670.
- [6] Y.W. Jun, J.S. Choi, J. Cheon, *Angew. Chem. Int. Ed.* 45 (2006) 3414–3439.
- [7] Y. Xia, Y. Xiong, B. Lim, S.E. Skrabalak, *Angew. Chem. Int. Ed.* 48 (2009) 60–103.
- [8] G. Liu, J.C. Yu, G.Q. Lu, H.-M. Cheng, *Chem. Commun.* 47 (2011) 6763–6783.
- [9] Q. Kuang, X. Wang, Z. Jiang, Z. Xie, L. Zheng, *Acc. Chem. Res.* 47 (2014) 308–318.
- [10] J.L. Giocondi, G.S. Rohrer, *J. Phys. Chem. B* 105 (2001) 8275–8277.
- [11] J.L. Giocondi, P.A. Salvador, G.S. Rohrer, *Top. Catal.* 44 (2007) 529–533.
- [12] Z. Zheng, B. Huang, J. Lu, X. Qin, X. Zhang, Y. Dai, *Chem. Eur. J.* 17 (2011) 15032–15038.
- [13] R. Li, F. Zhang, D. Wang, J. Yang, M. Li, J. Zhu, X. Zhou, H. Han, C. Li, *Nat. Commun.* 4 (2013) 2401.
- [14] C. Liu, X. Han, S. Xie, Q. Kuang, X. Wang, M. Jin, Z. Xie, L. Zheng, *Chem. Asian J.* 8 (2013) 282–289.
- [15] T. Ohno, K. Sarukawa, M. Matsumura, *New J. Chem.* 26 (2002) 1167–1170.
- [16] N. Murakami, Y. Kurihara, T. Tsubota, T. Ohno, *J. Phys. Chem. C* 113 (2009) 3062–3069.
- [17] H.G. Yang, C.H. Sun, S.Z. Qiao, J. Zou, G. Liu, S.C. Smith, H.M. Cheng, G.Q. Lu, *Nature* 453 (2008) 638–641.
- [18] A. Fujishima, X. Zhang, D.A. Tryk, *Surf. Sci. Rep.* 63 (2008) 515–582.
- [19] M.R. Hoffmann, S.T. Martin, W. Choi, D.W. Bahnemann, *Chem. Rev.* 95 (1995) 69–96.
- [20] O. Carp, C.L. Huisman, A. Reller, *Prog. Solid State Chem.* 32 (2004) 33–177.
- [21] X. Chen, S.S. Mao, *Chem. Rev.* 107 (2007) 2891–2959.
- [22] T. Froeschl, U. Hoermann, P. Kubiak, G. Kucerova, M. Pfanzelt, C.K. Weiss, R.J. Behm, N. Huesing, U. Kaiser, K. Landfester, M. Wohlfahrt-Mehrens, *Chem. Soc. Rev.* 41 (2012) 5313–5360.
- [23] B. Ohtani, Y. Ogawa, S.I. Nishimoto, *J. Phys. Chem. B* 101 (1997) 3746–3752.
- [24] H. Lin, C.P. Huang, W. Li, C. Ni, S.I. Shah, Y.H. Tseng, *Appl. Catal. B* 68 (2006) 1–11.
- [25] T. Tachikawa, S. Tojo, M. Fujitsuka, T. Sekino, T. Majima, *J. Phys. Chem. B* 110 (2006) 14055–14059.
- [26] D. Yang, H. Liu, Z. Zheng, Y. Yuan, J.C. Zhao, E.R. Waclawik, X. Ke, H. Zhu, *J. Am. Chem. Soc.* 131 (2009) 17885–17893.
- [27] M. Lazzeri, A. Vittadini, A. Selloni, *Phys. Rev. B Condens. Matter Mater. Phys.* 65 (2002), 119901–119901.
- [28] H.G. Yang, G. Liu, S.Z. Qiao, C.H. Sun, Y.G. Jin, S.C. Smith, J. Zou, H.M. Cheng, G.Q. Lu, *J. Am. Chem. Soc.* 131 (2009) 4078–4083.
- [29] G. Liu, H.G. Yang, X.-W. Wang, L. Cheng, H.F. Lu, Z. Wang, G.Q. Lu, H.M. Cheng, *J. Phys. Chem. C* 113 (2009) 21784–21788.
- [30] D. Zhang, G. Li, X. Yang, J.C. Yu, *Chem. Commun.* 29 (2009) 4381–4383.
- [31] X.Y. Ma, Z.G. Chen, S.B. Hartono, H.B. Jiang, J. Zou, S.Z. Qiao, H.G. Yang, *Chem. Commun.* 46 (2010) 6608–6610.
- [32] C.Z. Wen, J.Z. Zhou, H.B. Jiang, Q.H. Hu, S.Z. Qiao, H.G. Yang, *Chem. Commun.* 47 (2011) 4400–4402.
- [33] J. Pan, G. Liu, G.Q. Lu, H.M. Cheng, *Angew. Chem. Int. Ed.* 50 (2011) 2133–2137.
- [34] T.R. Gordon, M. Cargnello, T. Paik, F. Mangolini, R.T. Weber, P. Fornasiero, C.B. Murray, *J. Am. Chem. Soc.* 134 (2012) 6751–6761.
- [35] T. Tachikawa, S. Yamashita, T. Majima, *J. Am. Chem. Soc.* 133 (2011) 7197–7204.
- [36] M. D'Arienzo, J. Carballo, A. Bahamonde, M. Crippa, S. Polizzi, R. Scotti, L. Wabba, F. Morazzoni, *J. Am. Chem. Soc.* 133 (2011) 17652–17661.
- [37] Z. Bian, T. Tachikawa, P. Zhang, M. Fujitsuka, T. Majima, *J. Am. Chem. Soc.* 136 (2014) 458–465.
- [38] H. Cölfen, M. Antonietti, *Angew. Chem. Int. Ed.* 44 (2005) 5576–5591.
- [39] R.Q. Song, H. Cölfen, *Adv. Mater.* 22 (2010) 1301–1330.
- [40] (a) L. Zhou, P. O'Brien, *Small* 4 (2008) 1566–1574; (b) J. Fang, B. Ding, H. Gleiter, *Chem. Soc. Rev.* 40 (2011) 5347–5360.
- [41] Z. Bian, T. Tachikawa, P. Zhang, M. Fujitsuka, T. Majima, *Nat. Commun.* 5 (2014) 4038/4031–4038/4039.
- [42] Z. Bian, T. Tachikawa, T. Majima, *J. Phys. Chem. Lett.* 3 (2012) 1422–1427.
- [43] Z. Bian, T. Tachikawa, W. Kim, W. Choi, T. Majima, *J. Phys. Chem. C* 116 (2012) 25444–25453.
- [44] L. Zhou, D. Smyth-Boyle, P. O'Brien, *J. Am. Chem. Soc.* 130 (2008) 1309–1320.
- [45] T. Tachikawa, P. Zhang, Z. Bian, T. Majima, *J. Mater. Chem. A* 2 (2014) 3381–3388.
- [46] S. Sato, J.M. White, *Chem. Phys. Lett.* 72 (1980) 83–86.
- [47] S. Tabata, H. Nishida, Y. Masaki, K. Tabata, *Catal. Lett.* 34 (1995) 245–249.
- [48] E. Bae, W. Choi, *J. Phys. Chem. B* 110 (2006) 14792–14799.
- [49] S.K. Choi, S. Kim, J. Ryu, S.K. Lim, H. Park, *Photochem. Photobiol. Sci.* 11 (2012) 1437–1444.
- [50] M.M. Maitani, C. Zhan, D. Mochizuki, E. Suzuki, Y. Wada, *Catal. Sci. Technol.* 4 (2014) 871–877.
- [51] M.G. Walter, E.L. Warren, J.R. McKone, S.W. Boettcher, Q. Mi, E.A. Santori, N.S. Lewis, *Chem. Rev.* 110 (2010) 6446–6473.
- [52] (a) A. Kudo, Y. Miseki, *Chem. Soc. Rev.* 38 (2009) 253–278; (b) X. Chen, S. Shen, L. Guo, S.S. Mao, *Chem. Rev.* 110 (2010) 6503–6570.
- [53] N.O. McHedlov-Petrosyan, V.I. Kukhtik, V.D. Bezugliy, *J. Phys. Org. Chem.* 16 (2003) 380–397.
- [54] R.A. French, A.R. Jacobson, B. Kim, S.L. Isley, R.L. Penn, P.C. Baveye, *Environ. Sci. Technol.* 43 (2009) 1354–1359.
- [55] S.D.M. Islam, T. Konishi, M. Fujitsuka, O. Ito, Y. Nakamura, Y. Usui, *Photochem. Photobiol.* 71 (2000) 675–680.
- [56] J. Zhang, L. Sun, T. Yoshida, *J. Electroanal. Chem.* 662 (2011) 384–395.
- [57] D. Duonghong, J. Ramsden, M. Grätzel, *J. Am. Chem. Soc.* 104 (1982) 2977–2985.
- [58] R. Hengerer, L. Kavan, P. Krtil, M. Grätzel, *J. Electrochem. Soc.* 147 (2000) 1467–1472.
- [59] F. De Angelis, G. Vitillaro, L. Kavan, M.K. Nazeeruddin, M. Grätzel, *J. Phys. Chem. C* 116 (2012) 18124–18131.
- [60] J. Yu, J. Fan, K. Lv, *Nanoscale* 2 (2010) 2144–2149.
- [61] B. Laskova, M. Zukalova, L. Kavan, A. Chou, P. Liska, Z. Wei, L. Bin, P. Kubat, E. Ghadiri, J.E. Moser, M. Grätzel, *J. Solid State Electrochem.* 16 (2012) 2993–3001.
- [62] X.Q. Gong, A. Selloni, *J. Phys. Chem. B* 109 (2005) 19560–19562.
- [63] R.E. Tanner, A. Sasahara, Y. Liang, E.I. Altman, H. Onishi, *J. Phys. Chem. B* 106 (2002) 8211–8222.



- [64] (a) X.Q. Gong, A. Selloni, A. Vittadini, *J. Phys. Chem. B* 110 (2006) 2804–2811;  
(b) A. Vittadini, A. Selloni, F.P. Rotzinger, M. Grätzel, *Phys. Rev. Lett.* 81 (1998) 2954–2957.
- [65] T. Tachikawa, T. Majima, *Chem. Commun.* 48 (2012) 3300–3302.
- [66] N. Lakshminarasimhan, E. Bae, W. Choi, *J. Phys. Chem. C* 111 (2007) 15244–15250.
- [67] N. Lakshminarasimhan, W. Kim, W. Choi, *J. Phys. Chem. C* 112 (2008) 20451–20457.
- [68] S.K. Choi, S. Kim, S.K. Lim, H. Park, *J. Phys. Chem. C* 114 (2010) 16475–16480.
- [69] T. Tachikawa, M. Fujitsuka, T. Majima, *J. Phys. Chem. C* 111 (2007) 5259–5275.
- [70] W. Kim, T. Tachikawa, T. Majima, W. Choi, *J. Phys. Chem. C* 113 (2009) 10603–10609.
- [71] J.N. Clifford, E. Palomares, M.K. Nazeeruddin, M. Grätzel, J. Nelson, X. Li, N.J. Long, J.R. Durrant, *J. Am. Chem. Soc.* 126 (2004) 5225–5233.
- [72] G. Benkoe, J. Kallioinen, J.E.I. Korppi-Tommola, A.P. Yartsev, V. Sundstroem, *J. Am. Chem. Soc.* 124 (2002) 489–493.